PAPER

Check for updates

Temperature-responsive iron nanozymes based on poly(*N*-vinylcaprolactam) with multi-enzyme activity†

Yang Wang, [ID] *[a] Wei Wang,‡[c] Zhun Gu,[a] Xiangyang Miao,[a] Qiuyan Huang[a] and Baisong Chang*[b]

Iron (Fe)-based nanozymes are widely applied in the biomedical field due to their enzyme-like catalytic activity. Herein, Fe(II)-based coordination polymer nanohydrogels (FeCPNGs) have been conveniently prepared as a new type of nanozyme by the chelation reaction between ferrous iron and polymer nanohydrogels. The P(VCL-*co*-NMAM) nanohydrogels prepared by a reflux precipitation polymerization method using *N*-vinylcaprolactam (VCL) and *N*-methylol acrylamide (NMAM) as monomers and *N,N*-methylenebisacrylamide (MBA) as a crosslinker were esterified using P_2O_5 and then chelated with Fe(II) ions to form nanozymes with peroxidase and superoxide dismutase (SOD) activity. It was found by dynamic light scattering (DLS) and transmission electron microscopy (TEM) that the nanohydrogels prepared with a monomer concentration of 4% and mass ratio of 1 : 1 (VCL : NMAM) had more uniform particle size, better dispersion and a distinct temperature response. The results of Fourier transform infrared (FTIR), DLS, TEM, X-ray powder diffraction (XRD) and X-ray photoelectron spectroscopy (XPS) indicated the successful preparation of the esterified nanohydrogel and FeCPNGs. Of particular importance is that such FeCPNGs can functionally mimic two antioxidant enzymes (peroxidase and superoxide dismutase) by UV analysis of catalytic oxidation between 3,3,5,5-tetramethylbenzidine (TMB) and H_2O_2 and the kit analysis of SOD-like activity.

1 Introduction

Although natural enzymes play vital roles in biological reactions in living systems, their practical applications have been limited due to their easy denaturation or protease digestion, time-consuming preparation, high cost, and difficult recycling.[1,2] Compared with natural enzymes, the nanomaterial-based artificial enzymes named nanozymes possess better performance in controllable structure, tunable catalytic activities, and larger surface area for modification and bioconjugation, which results in broader application fields, including biosensing, immunoassays, cancer diagnostics and therapy, neuroprotection, stem cell growth, and pollutant removal.[3–6] Moreover, multiple functions could be endowed by introducing a smart response to external stimuli.[7–9]

The nanozymes mainly include materials such as metal oxides and sulfides, carbon materials or metal complexes, and their catalytic properties are mainly concentrated on oxidoreductases and hydrolases.[10] Acting as natural antioxidants, peroxidase and superoxide dismutase (SOD) are both enzymes that protect against oxidative stress correlated with reactive oxygen species (ROS), such as $O_2^{\bullet-}$, $OH^{\bullet-}$ and H_2O_2. Peroxidases are a typical category of enzymes which can catalyze oxidation of many organic substrates to reduce their toxicity, such as the oxidation of various metabolites and toxins by hydrogen peroxide (eqn (1)).[11] As written in eqn (2), SODs are a family of enzymes catalyzing the dismutation of $O_2^{\bullet-}$ into O_2 and H_2O_2.[12]

$$H_2O_2 + H_2R \rightarrow H_2O + R \tag{1}$$

$$2O_2^{\bullet-} + 2H^+ \rightarrow H_2O_2 + O_2 \tag{2}$$
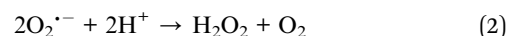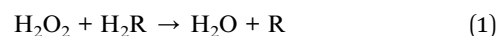
Iron-based nanomaterials, including iron oxides and sulfides, iron phosphate microflowers, and iron-based nanomaterials, reveal the increasing interest and efforts in the development of new nanozyme mimics[13–15] and have been widely used in the biomedical fields, such as cancer cell detection, blood glucose detection and immunoassay, *et al.* The methods used in synthesis of iron-based nanozymes mainly include co-precipitation method,[16] solvothermal method,[17]

[a]*Department of Medical Technology, Suzhou Chien-shiung Institute of Technology, Taicang 215411, Jiangsu Province, P. R. China. E-mail: 0070@csit.edu.cn*

[b]*State Key Laboratory of Advanced Technology for Materials Synthesis and Processing, Wuhan University of Technology, Wuhan, 430070, P. R. China. E-mail: chang@whut.edu.cn*

[c]*Nhwa Pharma. Corporation, Xuzhou 221000, Jiangsu Province, P. R.China*

† Electronic supplementary information (ESI) available. See DOI: 10.1039/d0ra07226e

‡ Co-first author.

hydrothermal method[18] and sol–gel method.[19] Iron phosphates (FePOs) as a well-known catalyst are used to selectively catalyze the oxidative dehydrogenation of saturated carboxylic acids and rapidly developed for catalytic applications. Wang *et al.* reported a facile method for the synthesis of iron phosphate microflower with peroxide and SOD enzyme activity.[14] In the report, $FeCl_2$, NaH_2PO_2 and polyvinylpyrrolidone (PVP) were first dissolved in glycol to form homogeneous solution and then transferred into an autoclave for generating microflowers. Tian and his coworkers prepared Fe(III)-based coordination polymer nanoparticles (FeCPNPs) with peroxidase-like activity by simple mixing of ferric chloride and sodium hexametaphosphate at room temperature.[20]

The nanozymes' surface coating is one of the common methods for enhanced stability and further bioconjugation.[21] However, the nanozymes' activity is usually decreased as the surface coating shields the catalytic nanozyme core from the substrates.[22] Numerous novel nanozymes combined with smart polymers have emerged with increasing considerable interest. Among the smart polymers, nanohydrogel is a kind of multiple dispersion system composed of lightly crosslinked three-dimensional polymer network structure and water,[23] and has gained accumulated attention due to the convenient functionalization of stimuli-responsive characters into nano-hydrogels.[24,25] Besides, the morphology and size of nanomaterials can be effectively controlled according to the different grid structure of the nanohydrogels on which the functional groups can also adsorb various metal ions and form metal nanozymes *in situ*.

As a class of thermosensitive nanomaterials, poly(*N*-vinyl caprolactam) (PVCL)-based nanohydrogels have been widely investigated in recent years owing to their sharp thermosensitive phase transition and better biocompatibility.[26,27] Precipitation polymerization is a commonly used synthetic method for preparation monodisperse nanohydrogels by mixing with monomers and initiators, followed by the precipitation of generated polymeric chains out of the continuous medium due to the low solubility in the selective reaction media and following conformation of the uniform particles.[28] The reflux precipitation polymerization (RPP) is a popular synthetic approach for fabricating monodisperse nanohydrogels modified from distillation precipitation polymerization (DPP) which undergoes the reactive condition in distilling state resulting in the formation of polymeric particles.[29] Compared with DPP, RPP might be a superior synthetic approach for preparing nanohydrogels by replacing distilling reaction apparatus with refluxing reaction apparatus, thus resulting in a wider range of monomers, higher colloidal stability, simpler operation and more desirable reaction efficiency.[30,31]

In this paper, a novel fabrication method for iron-based nanozymes is demonstrated for the first time that Fe(II)-based complexed polymer nanohydrogels (FeCPNGs) can be conveniently prepared by simple chelation reaction between ferrous irons and polymer nanohydrogels after esterification with P_2O_5. Polymer nanohydrogels (P(VCL-*co*-NMAM)) were prepared with reflux precipitation method by using *N*-vinylcaprolactam (VCL) and *N*-methylol acrylamide (NMAM) as monomers, *N,N*-
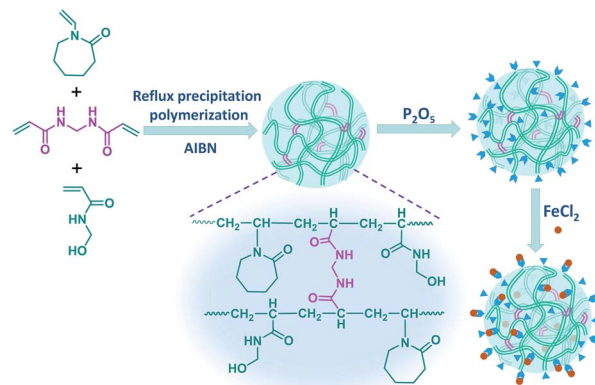
Scheme 1 The synthetic scheme of the iron nanozymes based on PVCL.

methylenebisacrylamide (MBA) as a crosslinking agent, azobisisobutyronitrile (AIBN) as an initiator (Scheme 1). The prepared nanohydrogels were used to phosphate with P_2O_5 and then chelated with Fe(II) to form catalytic microspheres (FeCPNGs) with peroxidase and SOD activity. The structure and properties of the nanohydrogels and nanozymes were characterized by dynamic light scattering (DLS), zeta potential, infrared spectroscopy (FTIR), transmission electron microscopy (TEM), X-ray powder diffraction (XRD), X-ray photoelectron spectroscopy (XPS). The enzyme catalytic activity was analyzed by ultraviolet spectrophotometer (UV), and superoxide dismutase (SOD) kits. The results suggest that such FeCPNGs manifested outstanding peroxidase and SOD-like enzymatic activity.

2 Experimental section

2.1 Materials

N-Vinylcaprolactam (VCL, 99%) was obtained from Sigma-Aldrich, *N*-methylol acrylamide (NMAM, 99%), *N,N*-methylenebisacrylamide(MBA, 99%) and azobisisobutyronitrile (AIBN, 99%) were purchased from Fluka and used as received. 3,3,5,5-tetramethylbenzidine (TMB), peroxidase from horseradish (HRP) (>300 units per mg), alizarin red reagent and H_2O_2 (30 wt%) were purchased from Aladin Ltd (Shanghai, China). Superoxide dismutase (SOD) kit was purchased from Nanjing Institute of Bioengineering. Acetonitrile, phosphorus pentoxide, anhydrous alcohol, tetrahydrofuran, isopropanol and anhydrous calcium chloride were analytically pure and obtained from Shanghai Chemical Reagents Company.

2.2 Characterization

Hydrodynamic diameter, zeta potential and light scattering intensity of the nanohydrogels and nanozymes were measured by using a dynamic light scattering (DLS) particle size analyzer (Malvern Nano-ZS90) at scattering angle of 90°. Fourier transform infrared (FTIR) spectra were obtained on a Nicolet Nexus-440 FT-IR spectrometer to confirm the chemical composition and structure information. X-ray diffraction (XRD, Rigaku D/

Table 1 Effect of different monomer mass ratios on the size of nanohydrogel

Sample[a]	NMAM (g)	VCL (g)	Mass ratio[b]	$D_h{}^c$ (nm)	PI[d]
P1	0.0702	0.5618	1 : 8	546.0	0.180
P2	0.0902	0.5417	1 : 6	619.6	0.211
P3	0.1264	0.5056	1 : 4	728.9	0.263
P4	0.2106	0.4213	1 : 2	776.0	0.192
P5	0.3160	0.3160	1 : 1	876.5	0.085
P6	0.4213	0.2106	2 : 1	990.9	0.626

[a] In the preparation reaction, the concentration of all monomers was 4% of total system, cross-linking agent was 20% of the total monomers, and the volume of the solvent AN was 20 mL. [b] Mass ratio was the mass ratio of NMAM and VCL. [c] The hydrodynamic diameter (D_h) was determined in 0.01 M phosphate buffer of pH 7.4 at 25 °C by DLS. [d] PI, polydispersity index of the particle size,[34] PI = $<\mu_2>/\Gamma^2$.

max 2550VB/PC diffractometer with Cu Kα radiation) and X-ray photoelectron spectroscopy (XPS, ESCALAB Xi⁺) were employed to confirm chemical composition and structure information of the nanozyme (FeCPNGs). Transmission electron microscopy (TEM) images were obtained on a Hitachi H-600 transmission electron microscope to characterize the morphology microstructure. UV-vis spectra were obtained using a PerkinElmer Lambda 35 spectrophotometer to analyze the catalytic oxidation activity to H_2O_2. The SOD inhibition rate and activity were measured with microplate assay (Multiskan Spectrum).

2.3 Preparation of P(VCL-co-NMAM) nanohydrogels

Reflux-precipitation polymerization was used to fabricate the P(VCL-co-NMAM) nanohydrogels. A typical procedure is as follows: an appropriate amount of VCL, NMAM and MBA (Tables 1 and 2), 0.0126 g azobisisobutyronitrile (AIBN) were dissolved in 20 mL of acetonitrile (AN) in a dried 50 mL triple-necked flask with reflux condenser. Afterwards, the reaction mixture was continuously heated to the boiling state within 30 min with stirring at the speed of 300 rpm. After constant reflux for 2 h, the reaction mixture was poured out and the generated nanohydrogels were separated and purified for three times by repeated centrifugation (5000 rpm for 15 min)/

Table 2 Effect of crosslinking agent dosage on nanohydrogel performance

Sample[a]	Dosage[b]	Crosslinker mass (g)	$D_h{}^c$ (nm)	PI[d]
PC1	10%	0.0632	551.1	0.133
PC2	15%	0.0948	760.1	0.209
PC3	20%	0.1264	876.5	0.085
PC4	25%	0.1580	1092.4	0.382

[a] In the preparation reaction, the mass ratio of NMAM and VCL was 1 : 1, total monomer dosage was 4% in respect to total system, initiator dosage was 2% of the total monomer mass, and the volume of the solvent AN was 20 mL. [b] Dosage of crosslinker was in respect to sum of NMAM and VCL. [c] The hydrodynamic diameter (D_h) was determined in 0.01 M phosphate buffer of pH 7.4 at 25 °C by DLS. [d] PI, polydispersity index of the particle size,[34] PI = $<\mu_2>/\Gamma^2$.

redispersion in anhydrous ethanol with the aid of ultrasonic bathing.

2.4 Phosphate esterification of P(VCL-co-NMAM) nanohydrogels

Phosphorus pentoxide (P_2O_5) was used to esterify with hydroxyl groups from P(VCL-co-NMAM) nanohydrogels. The specific procedure is as follows: 2 g nanohydrogels were dispersed in 30 mL tetrahydrofuran (THF) in a dried 50 mL triple-necked flask with the reflux condenser. After the aid of ultrasonic for 10 min, the emulsion was heated to 60–80 °C within water bath under magnetic stirring at 600 rpm, then anhydrous P_2O_5 was fed at intervals. After continuous reflux for 2–5 h, the mixture was poured out and purified for three times by repeated centrifugation (7000 rpm for 15 min)/redispersion in anhydrous tetrahydrofuran with the aid of ultrasonic bathing, then lyophilized to obtain a white fluffy powder.

2.5 Preparation of iron-based nanozymes (FeCPNGs)

1.5 g nanohydrogels esterified with P_2O_5, 20 mL absolute ethanol and 6 g or 7.5 g FeCl₂ were sequentially added into a 50 mL round-bottomed flask, then ultrasonically dispersed and heated to 60 °C with stirring at 400 rpm. After 2 h, the crude product was obtained by removing ethanol with a rotary evaporator, and then was washed with absolute ethanol which was subsequently evaporated to be removed. After lyophilization, a gray powdery product was obtained.

2.6 Thermo-sensitivity of P(VCL-co-NMAM) nanohydrogels

The temperature-sensitivity of the P(VCL-co-NMAM) nanohydrogels was respectively analyzed with DLS measurement by monitoring the change of hydrodynamic diameters with increasing temperature from 20–80 °C.

2.7 The composition detection of the esterified nanohydrogels

The nanohydrogels esterified with P_2O_5 mainly contain monoesters, diesters, small amounts of polyesters and free phosphoric acids. It is important to detect the content of monoester and diester in the products as more constituent diester may facilitate the next complexation reaction between phosphate and Fe(II) irons. Herein, the alizarin red S-phenolphthalein double indicator method was used to determine the content of mono- and di-esters. The specific steps are described as follows: 0.2 g (W_1) esterified nanohydrogels was dispersed in 5 mL isopropanol and 2 mL water with the aid of ultrasonic. Afterwards, appropriate amount of alizarin red reagent was added and shaken uniformly and then titrated with certain volume (V_1) of 0.1 mol L⁻¹ NaOH solution. Likewise, a certain amount of phenolphthalein indicator was added into the solution with another 0.2 g (W_2) esterified nanohydrogels, 5 mL isopropanol and 2 mL water. After uniform oscillation, a certain volume (V_2) of the same NaOH solution was used for titration to the end of the reaction, then a certain volume (V_3) of calcium chloride solution was used to make it fade back to colorless and then

titrate again to the end of the reaction. The calculation formulas are shown as the follows:

$$\text{Total acidity} = 56.1 \times 0.11 \times \frac{V_1}{W_1} \qquad (3)$$

$$\text{Content } (H_3PO_4) = (V_2 - V_3) \times 9.8 \times \frac{0.1}{W_2} \qquad (4)$$

$$\text{Content (monoester)} = \left[2 \times \frac{V_2}{W_2} - \frac{V_1}{W_1} \right] \times 0.1 \qquad (5)$$

$$\text{Content (diester)} = \left[2 \times \frac{V_1}{W_1} - \frac{V_2}{W_2} \right] \times 0.1 \qquad (6)$$

2.8 Thermo-sensitivity of esterified nanohydrogels and FeCPNGs

The temperature-sensitivity of the P(VCL-co-NMAM) nanohydrogels after esterification and FeCPNGs nanozymes was respectively analyzed with DLS measurement by monitoring the change of hydrodynamic diameters with increasing temperature from 20–65 °C.

2.9 Cytotoxicity assays

The cytotoxicity assay of FeCPNGs against HK-2 cells (human tubular epithelial cells, normal cells) was assessed by standard MTT assay for 48 h with different concentrations of nanozymes (1, 10, 100, 200, 500, 1000 μg mL^{-1}), and 0.15 M NaCl was used as control.

2.10 The analysis of peroxidase activity

The influence of different nanzyme concentrations on the catalytic effect as peroxidase was analyzed by the following procedures: 300 μL of a series of nanozyme dispersions with different concentrations of 0, 0.2, 0.4, 0.8, 1.2 and 1.6 mg mL^{-1} were respectively added into the mixture composed of 750 μL potassium phosphate buffer solution (1 mM, pH 4.0), 300 μL H$_2$O$_2$ solution (0.1 mM) and 150 μL TMB solution (4 mM), then the curves of absorbance versus wavelength were measured with a UV-visible spectrophotometer, and the change in absorbance at the maximum absorption wavelength was observed.

Effects of different H$_2$O$_2$ concentrations on the peroxidase catalytic reaction of nanozymes were analyzed by the following procedures: a series of H$_2$O$_2$ solutions with concentrations of 0, 0.05, 0.10, 0.15, 0.20, and 0.25 mM were prepared, and 300 μL of the above H$_2$O$_2$ solution was respectively added to the mixture of 750 μL acetate buffer (1 mM, pH 4.0), 150 μL TMB solution (4 mM), and 300 μL of enzyme dispersion(0.3 mg mL^{-1}). The curves of absorbance versus wavelength were measured with an ultraviolet-visible spectrophotometer, and the changes in absorbance at the maximum absorption wavelength was observed.

2.11 Kinetic analysis

The optimal concentration of FeCPNGs for kinetic analysis was determined as follows according to reported literature.[32] 50 μL of a series of nanozyme dispersions with different concentrations of 0.0, 0.2, 0.4, 0.6, 0.8, 1.0 and 1.2 mg mL^{-1} was respectively added into the mixture composed of 1.7 mL HAc–NaAc buffer solution (0.02 M, pH 4.0), 50 μL H$_2$O$_2$ solution (20 mM) and 200 μL TMB solution (4 mM), and the corresponding concentrations of the nanozyme in the reaction system were 0, 5, 10, 15 20, 25 and 30 μg mL^{-1}, respectively. The absorbance at 652 nm was recorded, and the enzyme concentration with the maximum ultraviolet absorption at 652 nm was the suitable concentration for kinetic analysis.

The enzyme kinetic assays were conducted by recording the absorbance at 652 nm at predetermined time intervals. 25 μg mL^{-1} FeCPNGs NPs, 0.4 mM TMB and 0.1–0.5 mM H$_2$O$_2$ were put into acetic acid (HAc)-sodium acetate (NaAc) buffer (pH 4.0, 0.02 M) at 25 °C. Similarly, 0.1 μg mL^{-1} HRP, 0.4 mM TMB and 0.1–0.5 mM H$_2$O$_2$ were put into HAc-NaAc buffer (pH 4.0, 0.02 M) at 25 °C as a control. The apparent kinetic parameters were calculated in the light of Lineweaver–Burk plots derived from Michaelis–Menten equation.[32]

2.12 The analysis of SOD activity

The SOD activity of the nanozymes was detected with the SOD kit according to the instruction of manufacturer. The specific operation steps are as follows: (1) open the SOD kit and prepare the corresponding enzyme working solution, diluent and substrate application solution according to the instructions, and then dilute the nanozyme dispersion to be tested to 0.2, 0.4, 0.6, 0.8, 1.0 and 1.2 mg L; (2) add the samples and operate the detection according to the illustration; (3) mix well and incubate at 37 °C for 20 minutes, and measure the absorbance at the wavelength of 450 nm by a microplate reader; (4) calculate the inhibition rate and activity of SOD according to the formula (7) and (8).

$$\text{Inhibition rate } (\%) =$$

$$\frac{A_{\text{control}} - A_{\text{control blank}} - (A_{\text{titration}} - A_{\text{titration blank}})}{(A_{\text{control}} - A_{\text{control blank}})} \times 100\% \qquad (7)$$

$$\text{Activity } (U \text{ mL}^{-1}) = \text{inhibition rate}\% \div 50\% \times \frac{0.24 \text{ mL}}{0.02 \text{ mL}} \qquad (8)$$

3 Results and discussion

3.1 Preparation of the P(VCL-co-NMAM) nanohydrogels

3.1.1 Effect of monomer ratio on nanohydrogel performance. The mass ratio of VCL and NMAM can result in the variation of the amount of hydroxyl groups on the surface, which has a great influence on the efficiency of the following esterification reaction. While keeping the other reaction conditions unchanged, DLS was used to determine the hydrodynamic diameter and dispersity of the nanohydrogels with
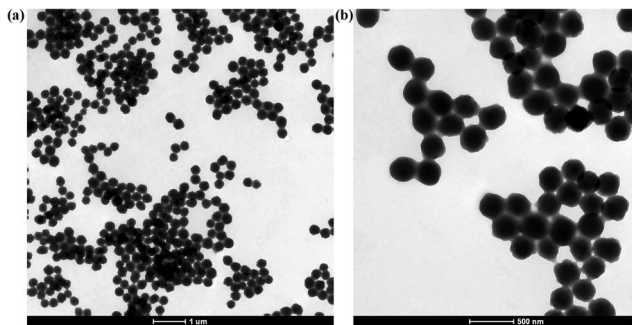
Fig. 1 TEM images of P(VCL-*co*-NMAM) nanohydrogels (m_{VCL} : m_{NMAM} = 1 : 1) with scale bars of 1 μm (a) and 500 nm (b), respectively.

Fig. 2 Response curve of the hydrodynamic diameter of the P(VCL-*co*-NMAM) nanohydrogel (m_{VCL} : m_{NMAM} = 1 : 1) as a function of temperature.

Fig. 3 Infrared spectrum of the P(VCL-*co*-NMAM) nanohydrogel.

increasing the mass ratio of NMAM and VCL from 1 : 8 to 1 : 6, 1 : 4, 1 : 2, 1 : 1 and 2 : 1. Table 1 and Fig. 1 showed that the sizes of the prepared particles became larger as the mass ratios of NMAM and VCL increased. The increase of hydroxyl groups from more NMAM in polymer chains brought about better hydrophilicity and resulted in larger particle sizes.[24] However, when the mass ratio exceeded 1 : 1, a larger size with poor particle dispersion appeared, which was because more hydrophilic NMAM resulted in longer chain length for precipitation, leading to larger particles and poor dispersion.[33]

Therefore, the nanohydrogels with monomer mass ratio of 1 : 1 were used for the next esterification reaction due to the better dispersibility and narrower particle size distribution.

3.1.2 Effect of the crosslinker amount on the nanohydrogel performance. The bisacryloyl cross-linking agent was utilized not only to make linear molecules form a network-like spherical structure, but also to increase the stability and rigidity of nanohydrogels. To research the influence of the cross-linking agent amount on the performance of nanohydrogel, the optimal amount of the cross-linking agent for preparing nanohydrogels was explored by changing the amount of cross-linking agent MBA from 10% to 15%, 20% and 25%. As shown in Table 2, the higher the amount of crosslinker, the larger the particle size. When the amount of MBA increased from 10% to 15% and 20%, the particle size of the nanohydrogels increased from 551.1 nm to 876.5 nm, indicating that more crosslinkers could make the initial cores catch more monomers and generate the larger particles in the polymerization system. Besides, more crosslinkers could result in the stronger cross-linking ability of the monomers and the greater hardness of the hydrogels. When the cross-linking dose was increased to 25%, the nanohydrogels no longer maintained stability, and began to aggregate and nucleate again, leading to much larger particle size, uneven distribution, and poor dispersion.[35]

3.1.3 The analysis of the nanohydrogel morphology. The TEM images of P (VCL-*co*-NMAM) nanohydrogels with the VCL and NMAM mass ratio of 1 : 1 were shown in Fig. 1. The nanohydrogels had a regular spherical morphology with uniform particle size from 241 nm to 333 nm. The particle size measured by TEM (280 nm) was smaller than that measured by
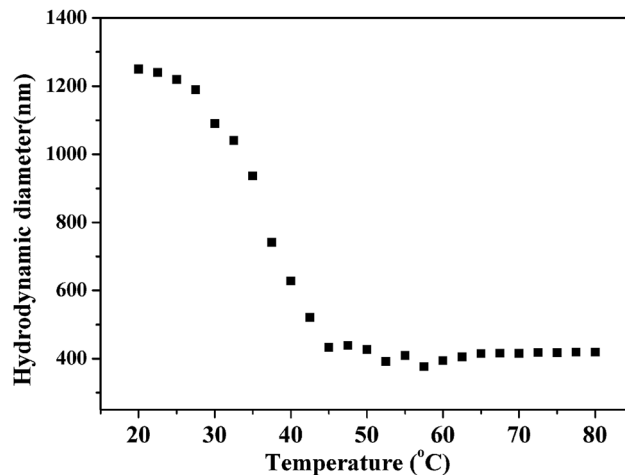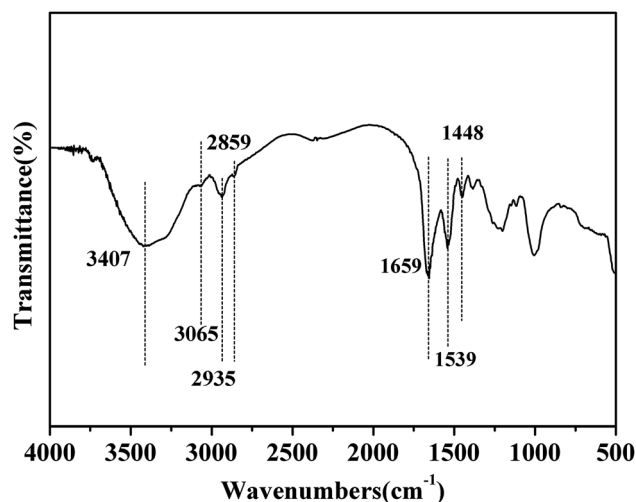
DLS (876 nm), which might be due to the swollen state in an aqueous solution at room temperature while the collapsed state for TEM observation.[34] The larger difference between the sizes measured by DLS and TEM indicated that the gel particles had more obvious swelling/shrinking ability.[36,37]

3.1.4 Temperature response analysis of nanohydrogel. Fig. 2 showed a response curve of the hydrodynamic diameter of the P(VCL-*co*-NMAM) nanohydrogel as a function of temperature. The results indicated that the prepared nanohydrogel shrank upon increasing the temperature as largely observed in the case of PVCL-based particles.[24,25] The observation of the size change from 1250 nm at 20 °C to 380 nm at 57.5 °C might originate from the poorer hydrophilicity of PVCL at higher temperature. When the temperature increased, PVCL changed from hydrophilic to hydrophobic,[38] and the particle size decreased rapidly. When the temperature exceeded 50 °C, the nanohydrogel size was almost unchanged even at 80 °C (420

Table 3 The effect of feed ratios of P_2O_5 and nanohydrogels on the esterified product composition

Mass ratio[a]	Monoester (mmol g^{-1})	Diester (mmol g^{-1})	Molar ratio[b]	H_3PO_4 (%)	Total acidity (mg KOH per g)
1 : 1	11.98	2.00	5.99	78.30	299.00
1 : 2	6.36	1.01	6.30	39.02	156.87
1 : 3	5.14	0.71	7.24	29.36	122.68
1 : 4	4.41	0.55	8.02	23.44	102.92

[a] Mass ratio in respect to P_2O_5 and nanohydrogels. [b] Molar ratio in respect to monoester and diester.

Table 4 Effect of reaction temperature on esterification

Temperature (°C)	Monoester (mmol g^{-1})	Diester (mmol g^{-1})	Molar ratio[a]	H_3PO_4 (%)	Total acidity (mg KOH per g)
60	7.19	0.61	12.97	39.17	157.18
65	5.45	0.85	6.41	32.56	133.84
70	6.36	1.02	6.24	39.02	156.98
75	5.73	1.12	5.10	35.23	149.20
80	6.16	0.82	7.51	39.02	145.76

[a] Molar ratio in respect to monoester and diester.

nm), indicating excellent stability at the reaction temperature of next esterification with P_2O_5.

3.1.5 Infrared spectroscopy (FT-IR) analysis. As shown in Fig. 3, the peaks appearing at 1659 cm^{-1} and 1539 cm^{-1} were respectively attributed to amide I and C–N bond belonging to the characteristic peaks of PVCL.[34] The bonds appearing at 2935, 2859 and 1448 cm^{-1} were attributed to stretching and bending vibrations of C–H groups, respectively.[39] Besides, the peak at 3407 cm^{-1} was attributed to the stretching vibration of –OH group originating from PNMAM,[40] inferring that NMAM had been successfully incorporated into the polymer network.

3.2 Phosphorylation of P (VCL-co-NMAM) nanohydrogels

3.2.1 Effect of P_2O_5 feed ratios on esterification. It is important to increase the diester composition of the esterified product to improve the efficiency of the subsequent complexing reactions.[41] Since the feeding amount and method of P_2O_5 may influence the product composition during esterification, P_2O_5 was fed in batches and the contents of mono- and di-esters were determined by the alizarin red S-phenolphthalein double indicator method. As shown in Table 3, the mono-ester content in the product rose with increasing amount of the P_2O_5 feeding, not beneficial to the subsequent complexation reaction with Fe(II). When the mass ratio of P_2O_5 and nanohydrogels was 2 : 1, large amounts of by-products appeared, which might be due to the excessive addition of P_2O_5, leading to local accumulation and overheating. When the mass ratio of P_2O_5 and nanohydrogels was 1 : 1, the amount of the generated diester was the highest, but increased content of free acid would retard the complexation reaction between the nanohydrogel and the Fe(II), so the esterified product with the 1 : 2 mass ratio of the P_2O_5 and the nanohydrogels was more suitable for the following complex reaction.

3.2.2 Effect of reaction temperature on esterification. It is very critical for esterification reaction to control reaction temperature precisely. As shown in Table 4, the composition of the esterified products prepared at different temperature (60, 65, 70, 75 and 80 °C) was determined by indicator titration to analyze the temperature effect on the product composition. The results illustrated that the diester content in the product increased first and then decreased when the esterification temperature rose. Likewise, the proportion of mono-diesters decreased first and then rose with increasing temperature, as shown in Fig. S1.† When the esterification temperature was 60 °C, the content of monoester and free phosphoric acid and total acidity were the highest while the diester content was lower and the proportion of mono- and di-ester was very high, which might be due to the inadequate reaction caused at the lower temperature. In comparison, when the temperature increased from 60 °C to 75 °C, the diester content increased and the proportion of monoester and diester decreased from 12.97 to 5.10, indicating facilitation of higher temperature on di-esterification. However, when the temperature increased to 80 °C, the reaction mixture became significantly darker, and the results of the decreased diester content and the increased proportion of mono- and di-esters implied the possible side reactions at a much higher temperature. In summary, 75 °C was the optimum temperature for the esterification.

3.2.3 Effect of reaction time on esterification. The reaction time also has a great influence on the diester content. Too short reaction time may lead to inadequate reaction in the system and lower product yield, while too long reaction time may result in increased by-products and decreased product purity. Therefore, different reaction time was selected to analyze the effect of reaction time on the ratio of mono- and di-ester. As shown in Table 5 and Fig. S2,† longer reaction time can promote the generation of the esterified products. Within 2–5 h, the diester

Table 5 The influence of reaction time on product composition

Reaction time (h)	Monoester (mmol g^{-1})	Diester (mmol g^{-1})	Molar ratio[a]	H_3PO_4 (%)	Total acidity (mg KOH per g)
2	5.63	0.48	11.73	33.79	123.26
3	5.68	1.17	4.85	35.07	149.80
4	6.36	1.02	6.24	39.02	156.98
5	5.69	0.85	6.69	35.37	138.20

[a] Molar ratio in respect to monoester and diester.
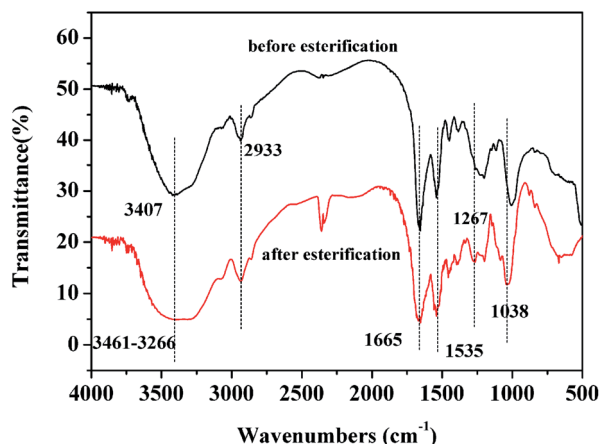
Fig. 4 Infrared spectra of nanohydrogels before and after esterification.

content first increased and then decreased, while the ratio of the mono- and diester first decreased and then increased, and the content of free acid remained almost unchanged. The above results may result from the higher activation energy required to form the diester compared to that of the monoester,[42] so the generation yield of the diester was lower than that of the monoester. When the reaction time reached 3 h, the diester content was the highest, while the esterification efficiency decreased due to the increased side reactions when the reaction

time continued to prolong. Therefore, 3 h was selected as the optimal reaction time for the esterification reaction.

3.2.4 Infrared spectroscopy (FTIR) analysis. The FTIR spectra of P(VCL-*co*-NMAM) nanohydrogels before and after esterification were shown in Fig. 4. The characteristic absorption peak of –OH at 3461–3266 cm^{-1} was attributed to the easy formation of hydrogen bonds between the molecules after the phosphorylation of the nanohydrogels, which resulted in a relatively broader peak at 3500–3200 cm^{-1}. 1665 cm^{-1} and 1535 cm^{-1} were attributed to the stretching vibration peaks of carbonyl C=O in the monomer. 1267 cm^{-1} and 1038 cm^{-1} were respectively attributed to P=O and P–O–C stretching vibration peaks,[43] indicating that the P(VCL-*co*-NMAM) nanohydrogels had been successfully esterified with P_2O_5.

3.3 Preparation of iron-based nanozymes (FeCPNGs)

3.3.1 The structural analysis of iron-based nanozymes (FeCPNGs). The zeta potential of the prepared nanozymes was used to characterize the P(VCL-*co*-NMAM) nanohydrogels, esterified nanohydrogels with P_2O_5, and nanozymes (FeCPNGs). As shown in Fig. 5, the zeta potential of the P(VCL-*co*-NMAM) nanohydrogels was slightly negatively charged due to the hydroxyl-rich surface of the NMAM-copolymerized nanohydrogels.[44] After esterification with P_2O_5, the potential decreased from −0.012 mV to −8.89 mV as the introduction of phosphate ions brought more negative charges on the surface of the nanohydrogels after esterification.[45] When the esterified nanohydrogels were complexed with Fe(II), the potential of the particles increased from −8.89 mV to 7.00 mV and 11.5 mV
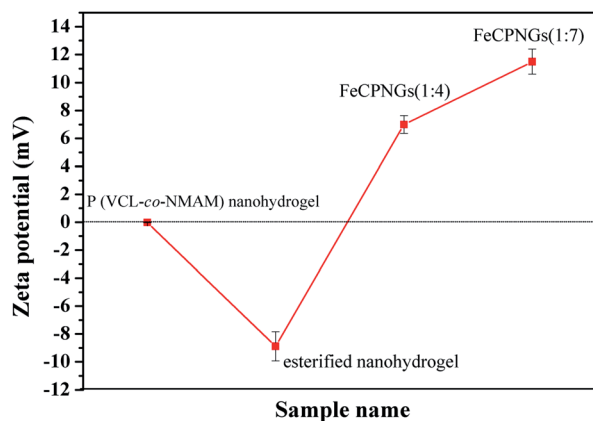

Fig. 5 Zeta potential of nanohydrogel, nanohydrogel after esterification and nanozymes with different mass ratios (1 : 4 and 1 : 7) of esterified nanohydrogel and $FeCl_2$.
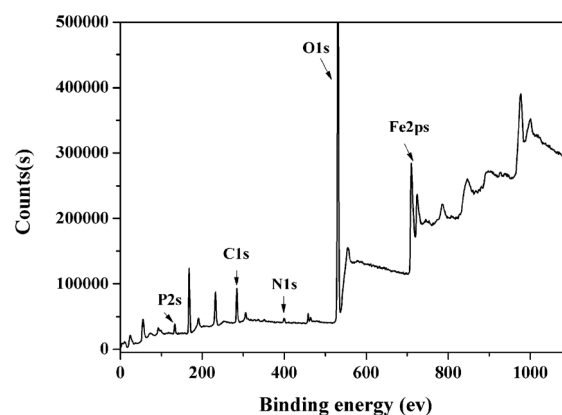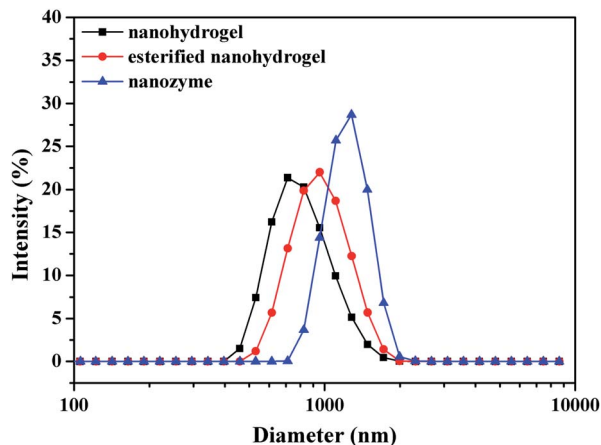

Fig. 6 Wide XPS spectrum of FeCPNGs.

Fig. 7 The diameter of P(VCL-*co*-NMAM) nanohydrogel (m_{VCL} : m_{NMAM} = 1 : 1), esterified nanohydrogel and nanozymes with mass ratio (1 : 7) of esterified nanohydrogel and FeCl$_2$.

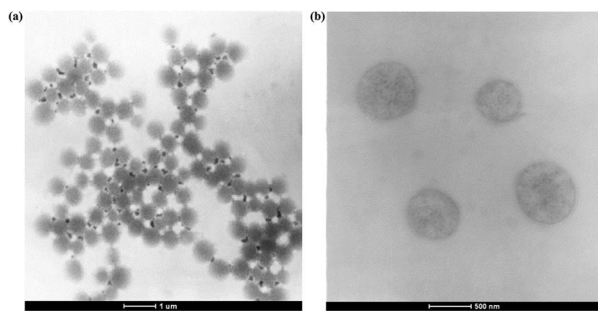**Fig. 8** TEM images with scale bars of 1 μm (a) and 500 nm (b) of FeCPNGs with mass ratio (1 : 7) of esterified nanohydrogel and FeCl$_2$.

(FeCPNGs(1 : 4) and FeCPNGs(1 : 7)), indicating more positive charges from increased amount of Fe(II) ions on the particle surface. Metal phosphate compounds are a large family of inorganic materials with the rich P–O coordination polyhedron and open skeleton structure.[46] In this work, P–O–Fe bonds were probably formed by bonding of iron with phosphate groups.[47] The XRD pattern of the FeCPNGs (Fig. S3†) showed the major diffraction peaks at 2θ = 18°, 28°, 34° and 36°, corresponding to the (200), (131), (041) and (241) facets of FeCPNGs, which was consistent with Fe$_3$(PO$_4$)$_2$·8H$_2$O[48] and FePOs.[14] Furthermore, XPS was used for evaluating the composition and element valence state of the FeCPNGs (Fig. 6). The peak (P2s) appearing at 133 eV suggested the formation of phosphate, and the distinctive peak (Fe2ps) at 710 eV indicated the existence of Fe(II) ions by complexation with FeCl$_2$.[49]

3.3.2 The size and morphology of iron-based nanozymes (FeCPNGs). Simultaneously, the size change of the nanohydrogels, esterified nanohydrogels, and FeCPNGs were shown in Fig. 7. The hydrodynamic diameter of the P(VCL-*co*-NMAM) (mVCL: mNMAM = 1 : 1) was 876.5 nm, and rose up to 983 nm after esterification with P$_2$O$_5$, then increased to 1246 nm, implying the success of esterification and iron complexation. After esterification, the phosphate anions on the surface of
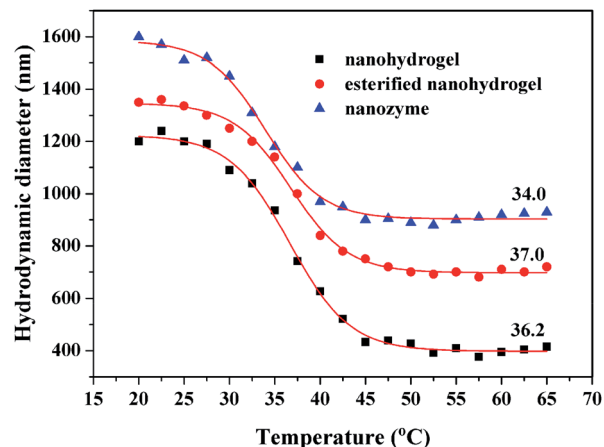

Fig. 9 The temperature responsive curves of the hydrodynamic diameter of FeCPNGs nanozyme and P(VCL-*co*-NMAM) nanohydrogel before and after esterification from 20 °C to 65 °C.

P(VCL-*co*-NMAM) nanospheres enhanced the hydrophilicity and electrostatic repulsion of the polymer chains in aqueous solution, resulting in an increase in particle size.[50] When chelated with Fe(II) ions, the generated complexes between Fe(II) ions and phosphate formed a certain thickness of coating, leading to a larger size.[51] The TEM images of FeCPNGs microspheres by phospholungstic acid stain shown in Fig. 8 also suggested the prepared nanozymes had larger particle size from 541 nm to 794 nm with regular spherical morphology. The microspheres for DLS measurement were swollen in the aqueous solution while those for TEM observation were collapsed and air-dried, which resulted in the larger DLS size than TEM size.

3.3.3 Temperature response analysis of FeCPNGs. It was reported that the volume phase transition temperature (VPTT) of PVCL-based nanogels was 31–38 °C,[52] and could be adjusted through the introduction of hydrophilic or hydrophobic components.[53] As shown in Fig. 9, the VPTT of the P(VCL-*co*-
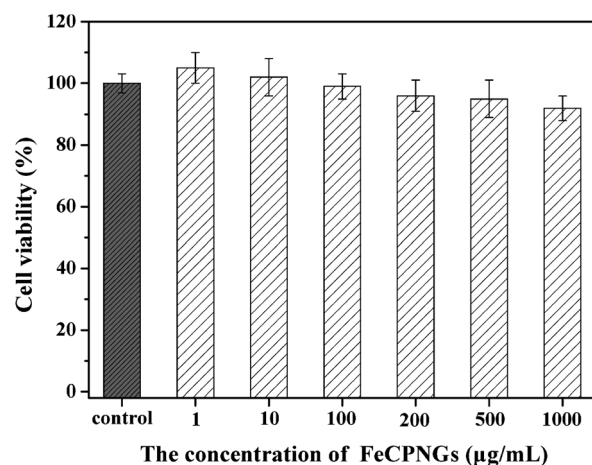

Fig. 10 Cell viability of HK-2 cell line incubated with different concentrations of nanozyme (FeCPNGs) for 48 h, the control is 0.15 M NaCl aqueous solution.

NMAM) (m_{VCL} : m_{NMAM} = 1 : 1) is 36.2 °C as hydrophilic hydroxyl groups improved the hydrophilicity of the polymer chains. After esterification, the phosphate anions on the surface of the P(VCL-co-NMAM) microspheres further enhanced the hydrophilicity and electrostatic repulsion of the polymer chains in aqueous solution, resulting in a higher temperature (VPTT, 37.0 °C) required to break the balance of hydrophilic and hydrophobic interactions between polymer chains.[54] When complexed with Fe(II) ions, the hydrophobicity was increased due to the generation of the P–O–Fe bonds,[47] leading to a lower VPTT.[54]

3.3.4 Cytotoxicity analysis. To evaluate the biocompatibility of FeCPNGs, the *in vitro* cytotoxicity assay against normal HK-2 cell line was conducted by treating the cells with FeCPNGs for 48 h. As shown in Fig. 10, no obvious cytotoxicity could be detected after 48 h incubation of FeCPNGs in the concentration range of 1–1000 μg mL^{-1}, and over 90% of cell viability was observed even up to the concentration of 1000 μg mL^{-1}. The low cytotoxicity of FeCPNGs may be ascribed to excellent biocompatibility of PVCL-based nanohydrogels.[25]

3.4 Analysis of enzyme catalytic activity

3.4.1 Analysis of peroxidase-like activity. On the basis of the peroxidase-like property of FeCPNGs, a colorimetric method for H_2O_2 detection was designed. As expected, the UV absorbance variation of TMB oxidation catalyzed by FeCPNGs was H_2O_2 concentration-dependent. In Fig. 11, there was almost no absorbance in the TMB + FeCPNGs system (black line), indicating that the reaction was very weak in the absence of H_2O_2. In contrast, there was an obvious absorption peak at 652 nm in the H_2O_2-TMB-nanozyme system. The above observation indicated that nanozymes could catalyze the oxidation of TMB to produce blue oxides as peroxide mimetic enzymes in the presence of H_2O_2. Fig. 11(a) showed the UV absorption curves in the presence of H_2O_2 with different concentrations (0, 0.05, 0.10, 0.15, 0.20, 0.25 mM) at the wavelength from 400 to 900 nm. Besides, the absorbance at 652 nm was proportional to the lower concentrations of H_2O_2 shown in Fig. 11(b). The value of R-Square was 0.9952, indicating favourable linear correlation. As is known that GOx can catalytically oxidizes glucose to gluconic acid, while the substrate oxygen is converted to H_2O_2. Subsequently, the generated H_2O_2 can be catalytically reduced by HRP in the presence of TMB co-substrate, leading to the characteristic blue color which can be tested by UV.[55] Therefore, the prepared FeCPNGs can replace HRP to determine the glucose concentration for diabetes detection. According to the same principle, the H_2O_2 in the milk sample can also be determined

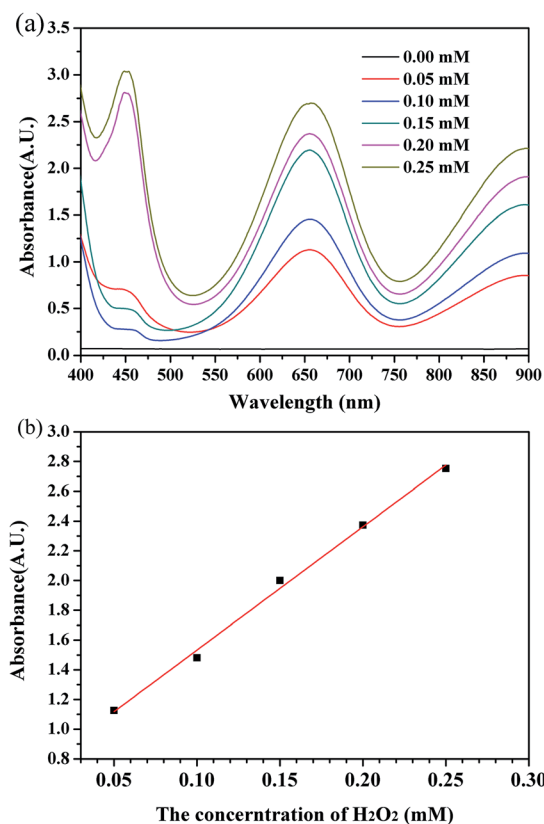**Fig. 11** Effect of different H_2O_2 concentrations (a) and linear relationship between H_2O_2 concentration and absorbance (b).

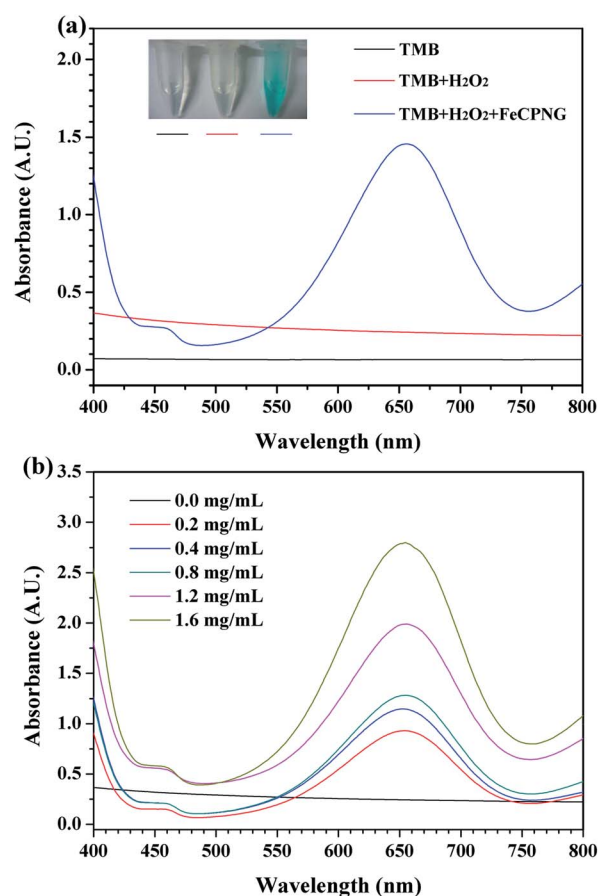**Fig. 12** (a) UV-vis spectra of TMB solution (black line), TMB + H_2O_2 (red line), TMB + H_2O_2 + FeCPNPs (blue line) (TMB: 4 mM; H_2O_2: 0.1 mM; FeCPNGs 0.3 mg mL^{-1}). Inset: typical photographs of three samples to the corresponding lines; (b) effect of different enzyme concentrations on the catalytic activity of TMB peroxidase.
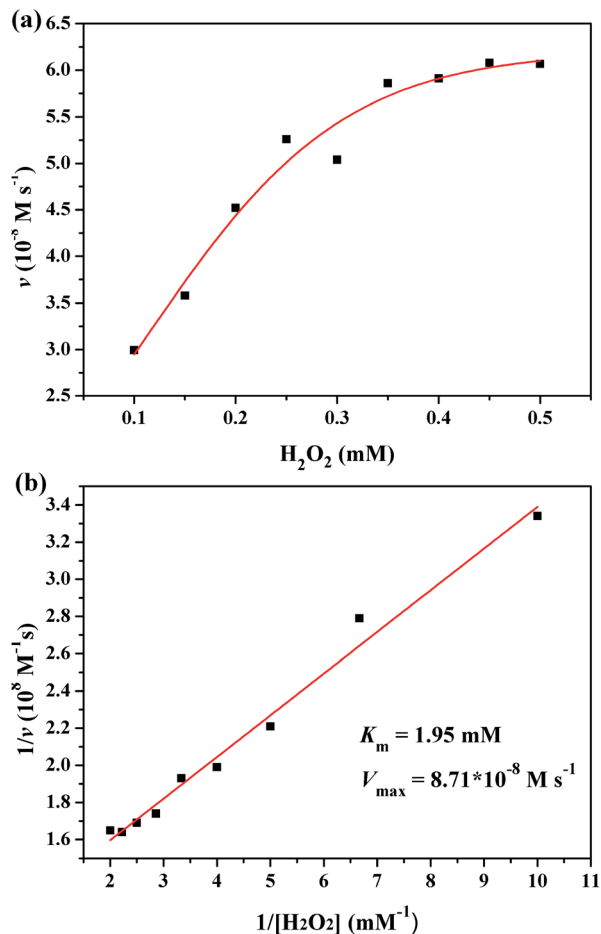
Fig. 13 Steady-state kinetic assays of the FeCPNGs. (a) The concentration of TMB was fixed as 400 μM, and H_2O_2 concentration was varied; (b) the Lineweaver–Burk plots of the double reciprocal of the Michaelis–Menten equation.

by centrifugation of milk sample to remove the organic substances such as protein, fat and so on.[48]

The inset in Fig. 12(a) showed the photographs of TMB solutions under different conditions. It could be seen that TMB solutions in the absence of H_2O_2 exhibited no color change, indicating that no bule oxides from TMB generated in the absence of FeCPNGs. However, after the addition of FeCPNGs into the solution containing H_2O_2 and TMB, a blue color was obviously observed after incubation, indicating that the FeCPNGs microspheres could catalyze the oxidation of TMB. The possible reaction mechanism might be explained with two cascade steps:[56] First, H_2O_2 was adsorbed onto the surface of FeCPNGs and the O–O bond was broken into ˙OH; Second, TMB was oxidized by ˙OH to form a blue-colored product. The corresponding absorption spectra were shown in Fig. 12(a), in which the absorbance peak localized at 652 nm originated from the oxidation of TMB.[57] Similarly, there was no absorbance in H_2O_2 + TMB system (black line in Fig. 12(b)), indicating that the reaction was hardly observed in the absence of nanozyme. The UV absorption curves at 400–800 nm were shown in Fig. 12(b) with the addition of different concentrations of enzyme

dispersions (0, 0.2, 0.4, 0.8, 1.2 and 1.6 mg mL^{-1}). The results showed that the higher concentration of the enzyme dispersion could promote catalytic oxidation between H_2O_2 and TMB, resulting in stronger absorption intensity at 652 nm.

3.4.2 Analysis of enzymatic kinetics. To better understand the mechanism of the peroxidase-like catalytic activity of FeCPNGs, the steady-state kinetics for TMB oxidation reaction was analyzed by comparing to that of horseradish peroxidase (HRP). Under the optimum conditions (details in Fig. S4 and S5†), a series of initial reaction rates were calculated and applied to the double reciprocal of the Michaelis–Menten equation.[58] From the Lineweaver–Burk plot, the key enzyme kinetic parameters such as maximum initial velocity (V_{max}) and Michaelis−Menten constant (K_m) were obtained and were given in Table S2.† The V_{max} value was a direct measure of the enzymatic catalytic activity, and the K_m value was considered as a specific reflection of enzyme affinity to substrates. A low K_m value indicated a strong affinity.[59,60] It could be observed that FeCPNGs (Fig. 13) and HRP (Fig. 14) followed the typical Michaelis−Menten model toward H_2O_2, so the Michaelis–Menten model could be used to evaluate the catalysis ability of

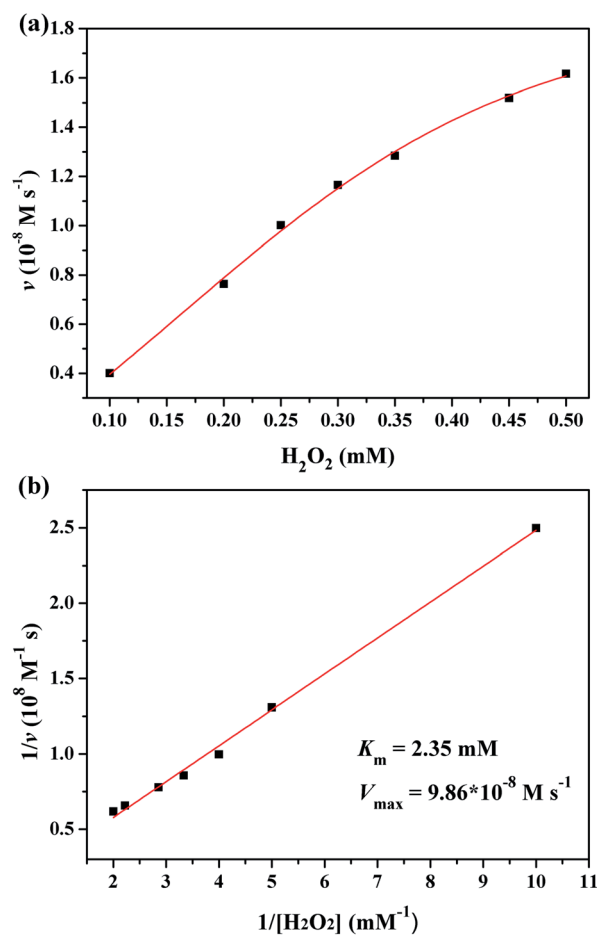**Fig. 14** Steady-state kinetic assays of HRP. (a) The concentration of TMB was fixed as 400 μM, and H_2O_2 concentration was varied; (b) the Lineweaver–Burk plots of the double reciprocal of the Michaelis–Menten equation.

FeCPNGs and HRP. In this work, the V_{max} was calculated to be 8.711×10^{-8} M s^{-1}, and the apparent K_m value of FeCPNGs with substrate H_2O_2 was calculated to be 1.95 mM, which was close to that of HRP (2.35 mM, Fig. 14), and much lower than that of Fe$_3$O$_4$ magnetic nanoparticles (154 mM)[61] and of Fe$_2$O$_3$ magnetic nanoparticles (324 mM),[62] indicating that FeCPNGs had excellent affinity to H_2O_2. The higher enzyme affinity to H_2O_2 could be ascribed to the existence of PO_4^{3-} on the surface of the microspheres as nonmetal oxyacid anions to contribute to electronic conduction and reaction with H_2O_2.[63] Besides, the complexation of Fe(II) with phosphate on the surface avoided the decrease of enzyme activity caused by surface coating.

3.4.3 The activity of SOD enzyme. Superoxide dismutase (SOD), an antioxidant enzyme[64] has been proved to play a very important role in preventing oxidative damage by anticancer and antiaging mechanisms.[65] As a diverse group of metalloenzymes, FeCPNGs can be used as superoxide dismutase (SODs) following the "pingpong" type catalytic mechanism of catalytic dismutation of the superoxide anion ($O_2^{\cdot-}$) to molecular oxygen (O_2) and hydrogen peroxide (H_2O_2).[66] The SOD kit used in this work utilized xanthine oxidase reaction system to generate superoxide anion free radicals which subsequently oxidized hydroxylamine to form formazan and could be measured with a visible light spectrophotometer at 450 nm. When the tested sample contains SOD, it has a specific inhibitory effect on superoxide anion free radicals and reduces the formation of nitrite, and the UV absorbance is lower than that of

the control.[67] From Fig. 15, the prepared nanozyme presented obvious SOD activity as expected, indicating that Fe(II) ions acted as reactive centers to catalyze the dismutation of $O_2^{\cdot-}$ into O_2 and H_2O_2. With the increase of concentration of H_2O_2 and nanozyme (Fig. 15), both the SOD inhibition rate and activity increased, suggesting that more H_2O_2 and nanozymes could enhance the SOD mimetic capability. The higher concentration of nanozyme increased the SOD inhibition rate and activity, which could be explained that the nitrite (formazan) was reduced due to the catalytic dismutation by FeCPNGs.[68] As H_2O_2 was the oxidation product of the xanthine, more additional H_2O_2 might have a higher specific inhibitory effect on superoxide anion free radicals and then reduced the formation of nitrite, resulting in a higher SOD activity.

4 Conclusions

In this report, a new type of Fe(II)-based nanozymes (FeCPNGs) exhibiting both peroxidase and SOD mimetic activities were prepared. With reflux precipitation polymerization method, P(VCL-co-NMAM) nanohydrogels were prepared and then esterified with P$_2$O$_5$ to introduce phosphate ions, which facilitated complexation with Fe(II) ions to form nanozymes. The DLS and TEM results showed that the size of the prepared P (VCL-co-NMAM) nanohydrogels increased with the mass ratio growth of VCL and NMAM and the amount of MBA, and that the nanohydrogels with the VCL and NMAM mass ratio of 1 : 1 and the MBA feeding amount of 20% were more suitable for the following preparation of nanozymes.

The FTIR results of the esterified products with P$_2$O$_5$ showed P=O and P–O–C stretching vibration peaks appeared respectively at 1267 cm^{-1} and 1038 cm^{-1}, indicating successful esterification with P$_2$O$_5$. The influencing factor analysis of the more generated diesters with the double indicator method showed 75 °C and 3 h was optimal reaction temperature and time, respectively.

As expected, the prepared nanozymes were proved to be successfully prepared through the characterization of zeta potential, size and morphology, XRD and XPS. The charge changes of the microspheres from negative (esterified nanogels) to positive (nanozymes) displayed successful complexation between esterified microspheres and Fe(II) ions. The prepared nanozymes showed better biocompatibility by cytotoxicity analysis and the regular spherical morphology with the larger size compared to that of the nanohydrogels before and after esterification.

Peroxidase-like activity analysis indicated the oxidation of peroxidase substrate TMB with H_2O_2 catalyzed by FeCPNGs nanozymes was recognized and provided a colorimetric assay for H_2O_2. Enzymatic kinetics analysis suggested FeCPNGs possessed corresponsive enzyme affinity to H_2O_2 compared to HRP. Further investigations on SOD-like activity demonstrated that Fe(II) ions acted as reactive centers to react with $O_2^{\cdot-}$ and showed SOD-like behavior. Inspired by the facial fabrication, cost effectiveness and dual-enzyme mimetic activities of peroxidase-like and SOD-like behaviors, FeCPNGs nanozymes
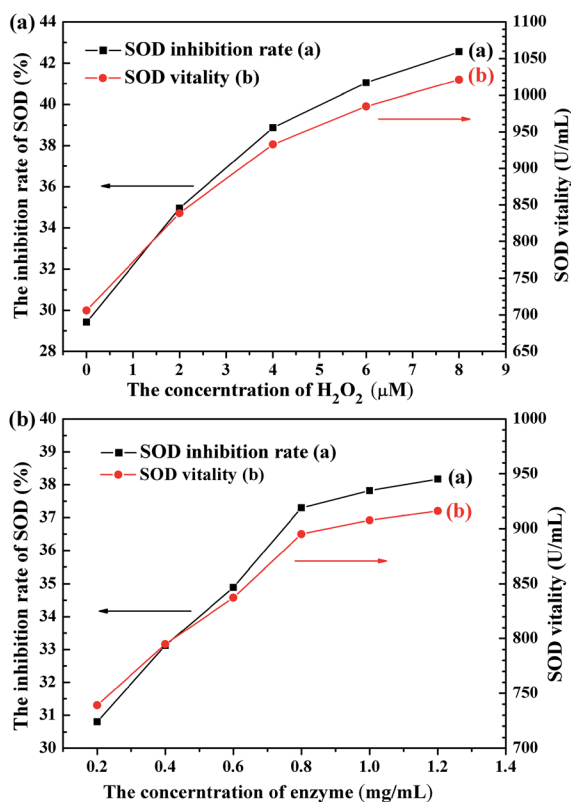

Fig. 15 Effect of different H$_2$O$_2$ (a) and nanoenzyme (b) concentrations on the inhibition rate and vitality of SOD.

are expected to be found applications as a biocatalyst or an antioxidant for clinical trials to fight ROS related diseases.

Conflicts of interest

There are no conflicts to declare.

Acknowledgements

Notes and references

1 H. Wei and E. Wang, *Chem. Soc. Rev.*, 2013, **42**, 6060.

2 A. Li, L. Ye, X. Yang and B. Wang, *ChemCatChem*, 2016, **8**, 3229.

3 J. Golchina, K. Golchina, N. Alidadian, S. Ghaderi, S. Eslamkhah, M. Eslamkhah and A. Akbarzadehd, *Artif. Cells, Nanomed., Biotechnol.*, 2017, **45**, 1069.

4 B. W. Yang, Y. Chen and J. L. Shi, *Prog. Biochem. Biophys.*, 2018, **45**, 237.

5 Y. Y. Huang, J. S. Ren and X. G. Qu, *Chem. Rev.*, 2019, **119**, 4357.

6 Y. H. Lin, J. S. Ren and X. G. Qu, *Acc. Chem. Res.*, 2014, **47**, 1097.

7 L. Gao and X. Y. Yan, *Prog. Biochem. Biophys.*, 2013, **40**, 892.

8 C. Luo, Y. Li and J. Long, *Sci. Sin.: Chim.*, 2015, **45**, 1026.

9 L. Z. Gao and X. Y. Yan, *Sci. China: Life Sci.*, 2016, **59**, 400.

10 J. Golchin, K. Golchin, N. Alidadian, S. Ghaderi, S. Eslamkhah and M. Eslamkhah, *Artif. Cells, Nanomed., Biotechnol.*, 2017, **45**, 1069.

11 J. M. Perez, *Nat. Nanotechnol.*, 2007, **2**, 535.

12 J. M. McCord and I. Fridovich, *J. Biol. Chem.*, 1969, **244**, 6046.

13 Q. M. Yang, S. Y. Lu, B. L. Shen and S. J. Bao, *New J. Chem.*, 2018, **42**, 6803.

14 W. Wang, X. P. Jiang and K. Z. Chen, *Chem. Commun.*, 2012, **48**, 7289.

15 Z. H. Dai, S. H. Liu, J. C. Bao and H. X. Ju, *Chem.–Eur. J.*, 2009, **15**, 4321.

16 S. L. Wei, J. W. Li and Y. Liu, *RSC Adv.*, 2015, **5**, 107670.

17 K. L. Fan, H. Wang, J. Q. Xi, Q. Liu, X. Q. Meng and D. M. Duan, *Chem. Commun.*, 2017, **53**, 424.

18 L. J. Wang, Y. Min, D. D. Xu, F. J. Yu, W. Z. Zhou and A. Cuschieri, *Chem. Commun.*, 2014, **50**, 11147.

19 Y. Gao, Z. Wei and F. Li, *Green Chem.*, 2014, **16**, 1255.

20 J. Q. Tian, S. Liu, Y. L. Luo and X. P. Sun, *Catal. Sci. Technol.*, 2012, **2**, 432.

21 B. w. Liu and J. w. Liu, *Nano Res.*, 2017, **10**, 1125.

22 L. Z. Gao, J. Zhuang, L. Nie, J. B. Zhang, Y. Zhang, N. Gu, T. H. Wang, J. Feng, D. L. Yang, S. Perrett and X. Yan, *Nat. Nanotechnol.*, 2007, **2**, 577–583.

23 Q. Y. Hu, P. S. Katti and Z. Gu, *Nanoscale*, 2014, **6**, 12273.

24 Y. Wang, G. J. Zhen, Y. F. Tian and W. L. Yang, *J. Mater. Chem. B*, 2015, **3**, 5824.

25 Y. Wang, J. S. Nie, B. S. Chang, Y. F. Sun and W. L. Yang, *Biomacromolecules*, 2013, **14**, 3034.

26 Y. D. Wu, S. Wiese, A. Balaceanu, W. Richtering and A. Pich, *Langmuir*, 2014, **30**, 7660.

27 A. Balaceanu, Y. Verkh, D. E. Demco, M. Moller and A. Pich, *Macromolecules*, 2013, **46**, 4882.

28 F. F. Sahle, M. Giulbudagian, J. Bergueiro, J. Lademann and M. Calderon, *Nanoscale*, 2017, **9**, 172.

29 P. Yang, D. Li, S. Jin, J. Ding, J. Guo, W. Shi and C. Wang, *Biomaterials*, 2014, **35**, 2079.

30 F. Wang, Y. Zhang, P. Yang, S. Jin, M. Yu, J. Guo and C. Wang, *J. Mater. Chem. B*, 2014, **2**, 2575.

31 M. L. Fan, F. Wang and C. C. Wang, *Macromol. Biosci.*, 2018, **18**, 1800077.

32 B. Jiang, D. M. Duan, L. Z. Gao, M. J. Zhou, K. L. Fan, Y. Tang, J. Q. Xi, Y. H. Bi, Z. Tong, G. F. Gao, N. Xie, A. F. Tang, G. H. Nie, M. M. Liang and X. Y. Yan, *Nat. Protoc.*, 2018, **13**, 1506–1520.

33 B. R. Saunders and B. Vincent, *Adv. Colloid Interface Sci.*, 1999, **80**, 1–25.

34 B. Chu, Z. L. Wang and J. Q. Yu, *Macromolecules*, 1991, **24**, 6832.

35 S. Jin, Y. J. Pan and C. C. Wang, *Acta Phys. Chim. Sin.*, 2013, **71**, 1500.

36 D. Boczula, A. Caly, D. Dobrzynska, J. Janczak and J. Zon, *J. Mol. Struct.: THEOCHEM*, 2012, **1007**, 220–226.

37 I. Varga, T. Gilanyi, R. Meszaros, G. Filipcsei and M. Zrinyi, *J. Phys. Chem. B*, 2001, **105**, 9071.

38 B. M. Dalton, S. C. Halligan, J. A. Killion, W. X. Wang, Y. X. Dong, M. J. D. Nugent and L. M. Geever, *Polym. Plast. Technol. Eng.*, 2018, **57**, 1165.

39 S. Shah, A. Pal, R. Gude and S. Devi, *Eur. Polym. J.*, 2010, **46**, 958–967.

40 W. J. Chuang and W. Y. Chiu, *Polymer*, 2012, **53**, 2829.

41 K. Hiroki, T. Sakagami, S. Masuhiro and O. Takeo, *J. Appl. Polym. Sci.*, 1998, **67**, 903.

42 A. J. Kirby, B. S. Souza and F. Nome, *Can. J. Chem.*, 2015, **93**, 422.

43 H. Chaair, H. Labjar and O. Britel, *Morphologie*, 2017, **101**, 120.

44 X. M. Mu and Z. S. Zhong, *Int. J. Pharm.*, 2006, **318**, 55–61.

45 Y. k. Sun, L. Duan, Z. R. Guo, Y. D. Mu, M. Ma, L. N. Xu, Y. Zhang and N. Gu, *J. Magn. Magn Mater.*, 2005, **285**, 65–70.

46 G. M. Wang, M. Valldor, B. Mallick and A. V. Mudring, *J. Mater. Chem. C*, 2014, **2**, 7417–7427.

47 G. Mali, M. Sala, I. Arcon, V. Kaucic and J. Kolar, *J. Phys. Chem. B*, 2006, **110**, 23060–23067.

48 J. J. Guo, Y. Wang and M. Zhao, *Talanta*, 2018, **182**, 230–240.

49 K. B. Yatsimirskii, V. V. Nemoshkalenko, Y. P. Nazarenko, V. G. Aleshin, V. V. Zhilinskaya and N. A. Tomashevsky, *J. Electron. Spectrosc. Relat. Phenom.*, 1977, **10**, 239–245.

50 F. Meeusse, E. Nies, H. Berghmans, S. Verbrugghe and F. E. Du Prez, *Polymer*, 2000, **41**, 8597–8602.

51 Y. D. Yang, Y. Liang, Z. X. Song and Q. G. Xian, *Inorg. Mater.*, 2005, **20**, 226–229.

52 A. Imaz and J. Forcada, *J. Polym. Sci., Part A: Polym. Chem.*, 2010, **48**, 1173–1181.

53 E. E. Makhaeva, H. Tenhu and A. R. Khokhlov, *Macromolecules*, 2002, **35**, 1870–1876.

54 T. Hoare and R. Pelton, *Langmuir*, 2004, **20**, 2123–2133.

55 X. L. Zuo, C. Peng, Q. Huang, S. P. Song, L. H. Wang, D. Li and C. H. Fan, *Nano Res.*, 2009, **2**, 617–623.

56 E. Kumacheva, *Adv. Mater.*, 2013, **25**, 132–136.

57 P. D. Josephy, T. Eling and R. P. Mason, *J. Biol. Chem.*, 1982, **257**, 3669–3675.

58 Y. L. Dong, H. G. Zhang, Z. U. Rahman and L. Su, *Nanoscale*, 2012, **4**, 3969–3976.

59 Y. Tao, Y. H. Lin, Z. Z. Huang, J. S. Reng and X. G. Qu, *Adv. Mater.*, 2013, **25**, 2594–2599.

60 A. Asati, S. C. Kaittanis, S. Nath and J. M. Perez, *Angew. Chem. Int. Ed.*, 2009, **48**, 2308–2312.

61 L. Z. Gao, J. Zhuang, L. Nie, J. B. Zhang, Y. Zhang, N. Gu, T. H. Wang, J. Feng, D. L. Yang, S. Perrett and X. Yan, *Nat. Technol. J.*, 2007, **2**, 577–583.

62 X. Q. Zhang, S. W. Gong, Y. Zhang, T. Yang, C. Y. Wang and N. Gu, *Mater. Chem.*, 2010, **20**, 5110–5116.

63 F. Zhang, Y. J. Shi, Z. S. Zhao, W. J. Song and Y. Cheng, *Appl. Surf. Sci.*, 2014, **292**, 570–575.

64 L. M. Walker, J. L. York, S. Z. Imam, S. F. Ali, K. L. Muldrew and P. R. Mayeux, *Toxicol. Sci.*, 2001, **63**, 143–148.

65 G. Giuseppa, A. Giuseppe, B. Francesco, R. Enrico and V. Graziella, *J. Inorg. Biochem.*, 2014, **131**, 56–63.

66 R. Patel, Y. A. Singh, N. Butcher, J. Jasinski, E. Colacio and M. Palacios, *New J. Chem.*, 2018, **42**, 3112–3136.

67 L. P. Nitha, R. Aswathy, N. E. Mathews, B. S. Kumari and K. Mohanan, *Spectrochim. Acta, Part A*, 2014, **118**, 154–161.

68 K. Korschelt, R. Ragg, C. S. Metzger, M. Kluenker, M. Oster, B. Barton, M. Panthöfer, D. Strand, U. Kolb, M. Mondeshki, S. Strand, J. Brieger, M. N. Tahir and W. Tremel, *Nanoscale*, 2017, **9**, 3952–3960.